Cathodoluminescence Modulation of ZnS Nanostructures by Morphology, Doping, and Temperature

Hui Liu, Linfeng Hu, Kentaro Watanabe, Xinhua Hu, Benjamin Dierre, Bongsoo Kim, Takashi Sekiguchi, and Xiaosheng Fang**

Spatially and spectrally resolved cathodoluminescence (CL) is one of the most effective methods to explore the optical properties of a nanomaterials and reveals the spatial distribution as well as the correlation between the luminescence and the sample morphology and microstructure. Here, CL modulation of ZnS nanostructures by controlled morphologies, Fe/Mn doping, and measurement temperature is demonstrated. High quality ZnS nanobelts and nanorods are synthesized on an Au-coated Si substrate and an Au-coated GaAs substrate via a facile thermal evaporation route. A room-temperature sharp ultraviolet (UV) lasing-like peak in various ZnS is achieved. The main UV luminescence peaks appear at wavelengths between 330 and 338 nm. The low temperature (32 K) CL spectrum consists of a narrow and strong UV peak centered at 330 nm and two broad, low-intensity peaks in the visible region (514 and 610 nm). Temperature-dependent CL from such single-crystalline ZnS nanobelts in the temperature range of 32 to 296 K reveals two UV peaks at 3.757 and 3.646 eV. The effects of Fe doping and Fe/Mn co-doping on the CL property of ZnS nanobelts are further investigated. These results imply that ZnS nanostructures can be used for potential luminescent materials as well as short-wavelength nanolaser light sources.

1. Introduction

One-dimensional (1D) inorganic semiconductor nanomaterials and nanostructures exhibit diverse and intriguing physical properties because of their reduced size and dimensionality compared to their bulk counterparts, rendering those subjects of great potential for both fundamental studies and future applications.[1–3] Especially, they can be used as ideal building blocks for a large variety of high performance nanodevices, such as field-effect transistors (FETs),[4] photodetectors,[5] photovoltaic devices,[6] biological and chemical sensors,[7] etc. Therefore, the controlled synthesis, unique properties and applications of various 1D nanostructures, such as nanowires, nanorods, nanotubes, nanobelts/nanoribbons, are becoming particular interest in recent decades. Zinc sulfide (ZnS), one of the first semiconductors discovered, has been widely used in electronic industry such as electroluminescence (EL), lasers, and as a light-emitting diode (LED) with doping because of its outstanding optical properties.[8] On the other hand, ZnS nanostructures have also attracted considerable interest due to their fascinating properties, such as a direct wide-band-gap (3.72 and 3.77 eV for cubic zinc blend (ZB) and hexagonal wurtzite (WZ) ZnS, respectively), the presence of polar surfaces, excellent transport properties, thermal stability and high electronic mobility.[9–13] A variety of interesting morphologies of the ZnS nanostructures with improved optical properties were synthesized, showing highly potential in ultraviolet (UV)-light sensors,[14,15] field emitters,[16] LED,[17] and biological applications.[18]

Among the various properties of ZnS nanostructures, the investigation of their optical properties is particularly important as they can absorb the fraction of the solar radiation which is carcinogenic for human. Additionally, while ZnS nanostructures are considered as one of the most suitable candidates for EL devices,[19] their use in multicolor displays with RGB emission has remained difficult as the materials for red, green, and blue phosphors require different processing conditions. Their luminous efficiencies, therefore, vary by up to an order of magnitude. Cathodoluminescence (CL) and photoluminescence (PL) are commonly used to study optical properties of a material, where CL is an optoelectrical phenomenon of light emission from a luminescent material caused by the material interacting with a beam of electrons generated by an electron gun, while PL is caused by the interaction between photon and materials. CL possesses many advantages over PL and other luminescence techniques. Higher spatial resolution (up to a few nm) and higher energy of electron beam make it suitable for exciting wide band-gap semiconductors. The CL image also allows the spatial distribution of excitonic states, defects, etc. to be directly

H. Liu, Dr. L. F. Hu, Prof. X. H. Hu, Prof. X. S. Fang
Department of Materials Science
Fudan University
Shanghai 200433, P. R. China
E-mail: hlf11@fudan.edu.cn; xshfang@fudan.edu.cn
Dr. K. Watanabe, Dr. B. Dierre, Prof. T. Sekiguchi
Advanced Electronic Materials Center
National Institute for Materials Science (NIMS)
Tsukuba, Ibaraki 305-0044, Japan
Prof. B. Kim
Department of Chemistry
KAIST, Daejeon 305-701, Korea

DOI: 10.1002/adfm.201203711

visualized.[20–23] Additionally, all the information got from CL can be interpreted along similar lines to those from other luminescence techniques, and emission lines associated with bound excitonic states, donor-acceptor pair bands and defect-related features typically dominate the spectra, with variations due to changes in alloying, strain, doping and carrier concentration all providing insights into the material properties.[20–24] These features favorably endows CL an excellent means to characterize nanomaterials and nanostructures.[22–24]

Large efforts devoted to study the optical properties of 1D ZnS nanostructures by using CL or PL so far have markedly improved the understanding of the optoelectronic transitions inside the ZnS nanostructures.[24–33] However, most of this research was either investigating the PL properties of 1D ZnS nanostructures, or only studing the CL properties for a given nanostructure at room temperature.[24,26–28,31–33] The changes of CL properties depending on the morphology, doping, and temperature remain unexplored. Since more detailed information on the near band-edge can be obtained at low temperatures, and the temperature changes can vary the interatomic distance, resulting in changes of the overlap among adjacent electronic orbitals and the structures of band energy, investigating the change of CL properties with temperatures may offer new information. Moreover, most of 1D ZnS nanostructures studied so far possess regular and uniform morphologies, and ones barely compared the difference of different individual nanostructures. Therefore, understanding the advantages and disadvantages of the irregular ZnS nanostructures may be useful to develop high performance nanodevices. Furthermore, most of the studies were concentrating on 1D pure ZnS nanostructures, and very few reports focused on doped ZnS nanostructures and compared the difference after doping as well as the difference between PL and CL properties of the same batch of samples. At the same time, there are still only very few reports on the UV near band-edge emission of 1D ZnS nanostructures at room temperature unlike its bulk form.[24–27] This is mainly caused by the fact that the optical properties of 1D ZnS nanostructures are very sensitive to the synthetic conditions, their crystal shape and size, impurities, and intrinsic defects, such as vacancies, interstitials, and others. Nevertheless, understanding the nature of defect states and how to control them on purpose to get the near band-edge emission at room temperature are of prime importance for future development of 1D nanostructures based nanodevices. In order to address these aforementioned issues, we herein have systematically studied morphology, doping, and temperature-dependent CL modulation of ZnS nanostructures. 1D ZnS nanostructures with different morphology and size exhibit sharp UV band-gap emission centered at wavelengths between 330 and 338 nm at room temperature. CL observations from single-crystalline ZnS nanobelts are investigated at low temperature (32 K). Temperature-dependent (32 to 296 K) CL spectroscopy of nanobelts and nanorods has been performed, and the origin of UV and visible band emission was studied and interpreted. The effects of Fe doping and Fe/Mn co-doping on CL property of ZnS nanobelts are further investigated. The present results should be not only useful for understanding the mechanism of the light emission and rational design of nanodevices of ZnS nanostructures, but also for envisaging the modulation route on other inorganic semiconductor nanostructures.

2. Results and Discussion

Figure 1a,b show the typical transmission electron microscopy (TEM) image and its corresponding high-resolution TEM (HRTEM) image near the edge of a single ZnS nanobelt, unveiling a peculiar rectangular geometry with sharp corners, smooth surface and a clear two-dimensional lattice fringe. This result suggests that the ZnS nanobelts are structurally uniform and free of defects such as dislocations. The sharp contrast of the diffraction dots showing the selected-area electron diffraction (SAED) pattern in Figure 1b also indicates that the nanobelt is highly crystallized. The marked interplanar *d* spacings of ≈0.63 and ≈0.33 nm in the HRTEM image correspond to the (0001) and (01–10) lattice planes of the wurtzite-2H ZnS (JCPDS No. 36–1450), respectively, which is consistent with the X-ray diffraction (XRD) pattern (not shown here), revealing that the nanobelt has grown along the [01–10] direction (see the white arrow in Figure 1b). Since the nanobelt lay flat on the copper grid during the TEM observation and the direction

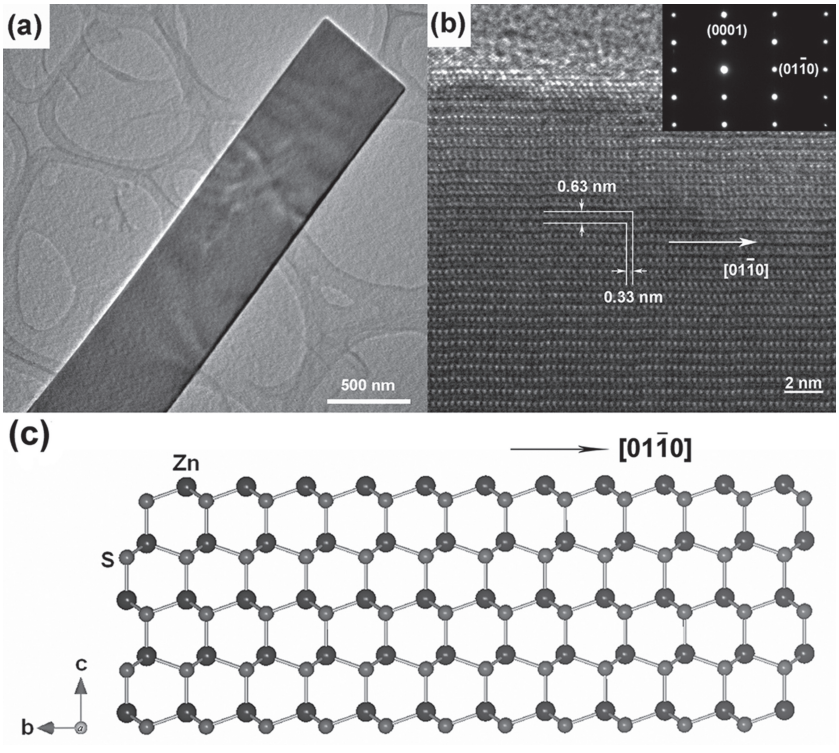

Figure 1. a) TEM image of a typical ZnS nanobelt and b) HRTEM image and its corresponding SAED pattern (inset). c) Atomic structural model of the nanobelt.

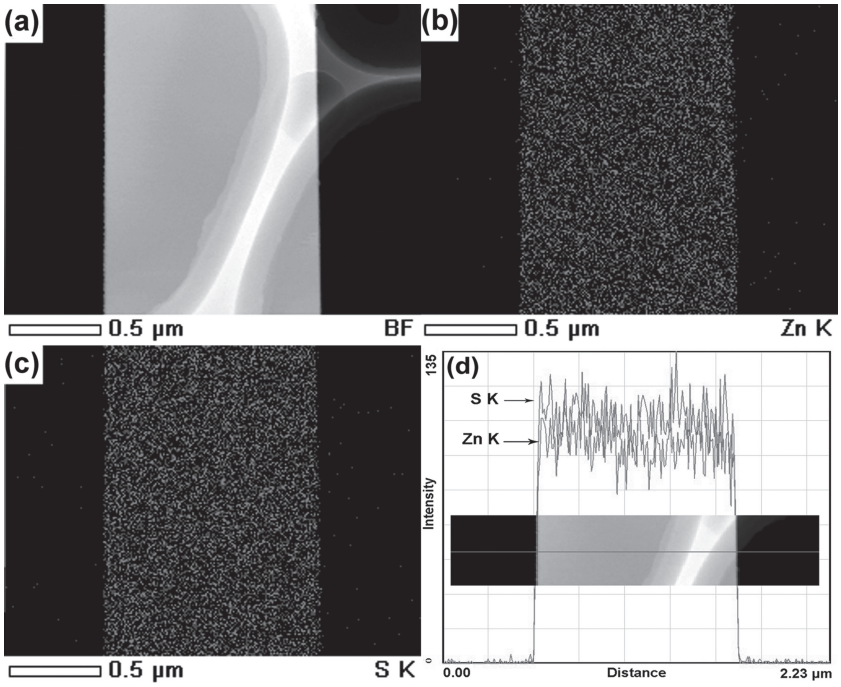

Figure 2. a) HAADF STEM image and the corresponding EDS element maps for b) Zn and c) S. d) EDS line scan along the straight line (inset) showing Zn and S profiles through an individual ZnS nanobelt.

of the electron beam is perpendicular to the nanobelt, one can conclude that each ZnS nanobelt is a single crystal with a (–2110) surface. Figure 1c schematically shows the atomic configuration of the surface of the belt, indicating that the side planes are polar surfaces and terminated either with Zn or S atoms.

Statistics based on numerous scanning electron microscopy (SEM) and transmission electron microscopy (TEM) observations indicates that most of the as-synthesized ZnS nanobelts possess regular and uniform morphologies with typical widths of 200 nm to 2 μm and lengths of up to a few millimeters. In order to further analyze the chemical composition and elemental distribution of the nanobelt, a detailed chemical analysis was carried out on an individual ZnS nanobelt using EDS elemental mappings and line-scanning elemental mapping (indicated by a straight line), as shown in **Figure 2**. From the X-ray energy dispersive spectroscopy (EDS) elemental maps in Figure 2b,c, one can see that the distribution of Zn and S elements is rather uniform, which clearly shows the shape of its high angle annular dark field (HAADF) scanning transmission electron microscopy (STEM) image (Figure 2a). The elements distribution along the line in Figure 2d also conveys the information that Zn and S are homogeneously distributed within the nanobelt.

Figure 3a,b show a typical TEM image of an individual ZnS nanorod grown on GaAs (111) substrate at 850 °C with a uniform shape and its corresponding HRTEM image, respectively. There is no appreciable amorphous phase on the edge. The clear lattice fringes in Figure 3b confirm that the nanorod is single crystalline. The SAED pattern in the inset of Figure 3b exhibits regularly arranged sharp diffraction spots without any secondary spots, and the marked interplanar d spacings are ≈0.19 and ≈0.31 nm which can be indexed to the (11–20) and (0002) planes of a hexagonal wurtzite-2H ZnS (JCPDS No. 36–1450) crystal, respectively, indicating the nanorod grows along the [0001] direction, as marked with a white arrow. Figure 3c depicts the atomic structure of the nanorods. The growth direction along the polarized [0001] plane is well illustrated. The elemental maps and line-scanning elemental mapping of a single ZnS nanorod are presented in **Figure 4**. The results show the distinct shape of a single nanorod without any partial aggregation, conveying information that Zn and S elements are homogeneously distributed in the nanorod.

The present nanorods possess the same hexagonal wurtzite-2H structure as nanobelts, consisting with the result that higher temperature favors wurtzite phase,[10] but they grew along different directions. Although much work has been done to study the fundamental

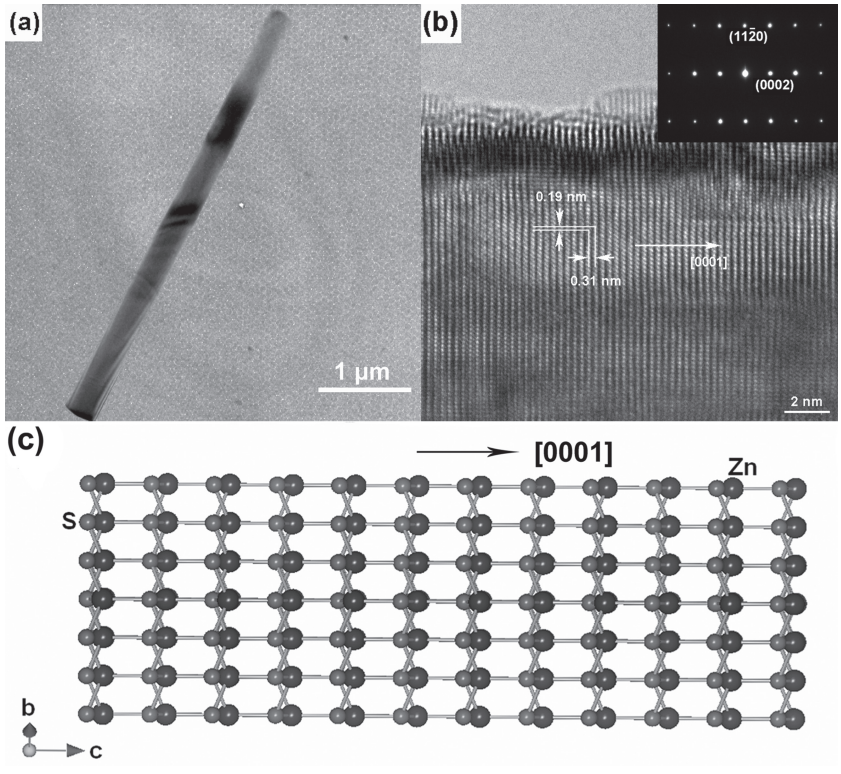

Figure 3. a) Typical TEM image of a single ZnS nanorod and b) HRTEM image and its corresponding SAED pattern (inset). c) Atomic structural model of the nanorod.

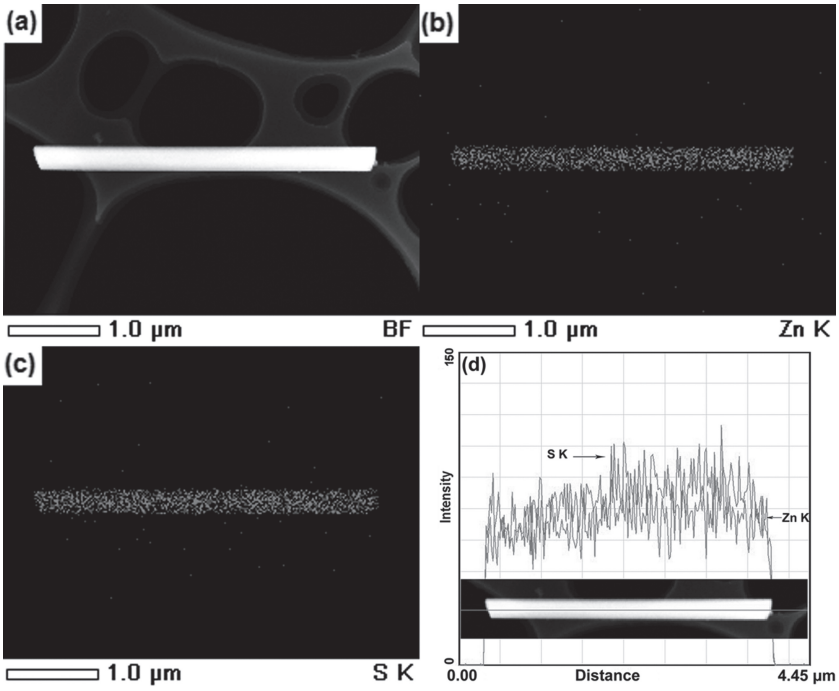

Figure 4. a) HAADF STEM image and the corresponding EDS element maps for b) Zn, and c) S. d) EDS line scan along the straight line (inset) showing Zn and S profiles through a single ZnS nanorod.

properties and potential applications of 1D ZnS nanostructures, the growth mechanism is still staying ambiguous due to their extremely complex growth thermodynamics and kinetics. Most of the growth direction documented in literatures is along [0001] for both nanobelts and nanorods,[12,16,25–28] whereas the [01–10] orientation is also an alternative growth direction for the nanobelts when the synthesis conditions are changed.[13,14,33] The growth direction is along [01–10] of the nanobelts, indicating that the polar surfaces play a relatively less important role in determining the final morphology in this case.[11] Generally, the wurtzite nanorods grown with the assistance of a metal catalyst have a preferential growth direction along the c-axis, the [0001] crystal direction.[27] However, the six equal planes of ±(11–20), ±(-2110) and ±(1–210) of ZnS with hexagonal symmetry have the lowest surface energy, favoring the formation of this type of low-energy nanobelt growing along the [01–10] direction with the lowest energy.[13] For the nanobelts, the Au film deposited on the substrate and high temperature (1100 °C) must also play an important role in the growth direction [01–10]. As mentioned in our previous report,[14] the ZnS nanobelts grew from some "seed" on the substrate, and these "seed" offer nucleation centers for the nanobelt growth as well as restrict their further growth along a given growth direction [01–10].

The overall CL properties of several nanobelts are shown in **Figure 5**. The CL image of the nanobelts in Figure 5b exhibits the corresponding shape in Figure 5a, indicating the luminescence is fairly uniform. Figure 5c shows the CL spectrum at 32 K of the ZnS nanobelts, consisting of a strong UV band centered at ≈330 nm (3.758 eV) and two visible bands at ≈514 nm (2.412 eV) and ≈610 nm (2.033 eV). The research on optical properties of 1D ZnS nanostructures has widened rapidly in recent years, and the near band-edge emission (330 nm to 345 nm, 3.594 eV to 3.758 eV) and the visible emission (400 nm to 580 nm, 2.138 eV to 3.100 eV) have been plentifully reported.[24–33] **Table 1** summarizes the UV range emissions of ZnS nanostructures and films.[20,25,29,34–36] The present UV emission shows an unsymmetrical shape, which should be decomposed into several Gaussian bands associated with different transitions. The inset shows the deconvolved spectrum with two peaks centered on 3.757 eV and 3.646 eV, these values are very close to the value of 3.754 eV and 3.662 eV respectively compared with these emissions. So these two peaks can be attributed to the recombination of exciton bond to a neutral acceptor (A^0X) and from free electrons in the conduction band to an acceptor level (e, A). The emission band centered at 514 nm (2.412 eV) at 32 K, and it shifts to 527 nm (2.353 eV) as the temperature rises up to 296 K. Besides, this emission band is located around 543 nm (2.284 eV) of other individual nanobelts, as shown in the following sections. Mitsui et al. also reported the emission of 527 nm (2.353 eV) in ZnS/GaAs films at room temperature.[20] They pointed out that such emission may be associated with point defects, which is most likely the isolated Zn vacancy in the single negative charge state. Wang et al. observed the emission of (546 nm) 2.271 eV and understood it as the Au impurity-related deep level emission in their nanowires which were synthesized with the assistance of Au catalyst.[31] Li et al. observed a strong emission centered at 2.300 eV in wurtzite ZnS nanobelt at room temperature using CL.[33] However, the emission band of 610 nm (2.033 eV) is seldom documented from PL measurement. It may be caused by oxygen impurity, which has been observed in ZnS nanowires using CL by Lee et al. that shows the energy and the relative intensity of such emission bands can differ at different spots of the sample.[24] It is notable that the incident electron beams of CL possesses much higher energy (three or four orders) compared to PL, and the interaction between electron beam and sample can take place within a very short time of around 10 ps.[37,38] Thus, the high electron beam energy (10 kV and 2000 pA) during the CL measurement may cause the bond breaking in ZnS nanobelts, and then the formation of reactive sites. These reactive sites can react with absorbed gas from the SEM chamber, such as residual O atoms, and form new defect midbands.[39,40]

In order to provide further insight of these emission states, CL emission at different temperatures from 32 K to 296 K were performed, as shown in Figure 5d. It can be seen that when the temperature is higher than 120 K (i.e., from 190 K to 296 K), the two UV peaks of 3.757 eV and 3.646 eV disappear, and another peak around 3.840 eV appears. This peak can be assigned to free exciton B (FXB).[25] The peak positions of the UV band changing with temperature are depicted in **Figure 6**a. The absence of A^0X and (e, A) is consistent with the results

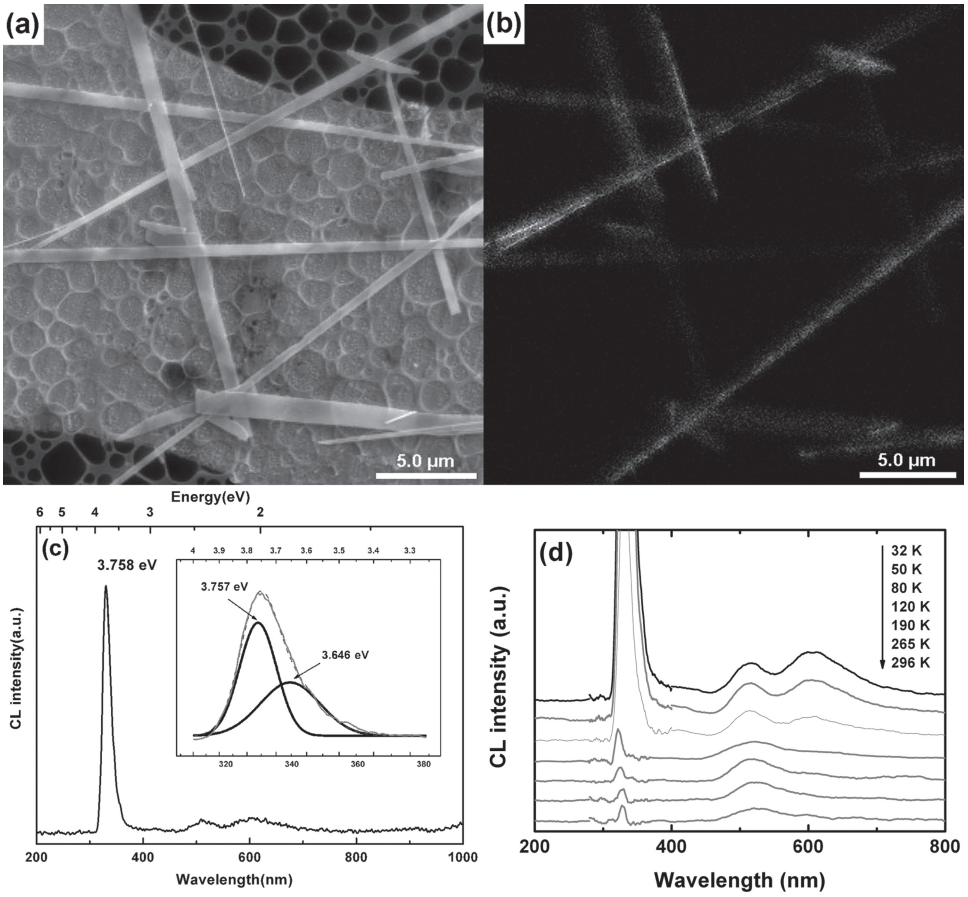

Figure 5. a) SEM image of ZnS nanobelts and b) their corresponding CL image. c) The CL spectrum at 32K, the inset is the enlarged spectrum and its Gaussian fitting (solid lines) from 310 nm to 360 nm. d) CL spectra from 32 K to 296 K.

that both A^0X and (e, A) thermally dissociated below 120 K,[34] and the existence of FXB may be caused by the high energetic electron beams of CL, the energy is not enough to excite FXB when the temperature is lower than 120 K. However, when the temperature increases, the increase of thermal energies results in the exciting of FXB and the decomposition of A^0X and (e, A). It is known that the peak positions shift to lower energy as a result of thermal dilation of the lattice as well as the electron-phonon interaction, as shown in Figure 6a. For the emission band around 514 nm (2.412 eV), the temperature dependence of photon energy is fitted to the extended phenomenological Varshni equation as shown in Figure 6b.[34]

Table 1. Near band-gap emissions of ZnS nanostructures and films

FXC	FXB	FXA	FXA-LO	D^0X	A^0X	A^0X-LO	(e, A)	(e, A)-LO	Temperature, type	Ref.
3.850	3.745	3.676	–	–	–	–	–	3.620	Nanowire, RT, PL	[25]
–	3.844	3.778	–	–	–	–	–	–	Nanowire, 10 K, PL	[25]
–	3.827	3.812	3.772	–	–	–	–	3.624	Nanobelt, 10 K, PL	[29]
–	–	–	–	3.782	–	–	3.665	3.626	Nanowire, 10 K, PL	[29]
X_{hh}		X_{lh}		D^0X	A^0X	A^0X-LO	(e, A)	(e, A)-LO	Temperature, type	Ref.
3.800		3.795		3.786	3.734	–	3.662	–	Film, 10 K, PL	[34]
–		3.787		–	3.754, 3.744, 3.729	3.689	3.662	–	Film, 10 K, PL	[35]
3.799		3.797		3.794, 3.792, 3.789	3.754, 3.744, 3.740	3.710	3.668	–	Film, 10 K, PL	[36]
–		–		3.787	3.741	–	3.652	3.625	Film, 20 K, CL	[20]
–	3.840	–	–		3.757	–	3.646		Nanobelts, 32 K, CL	This work

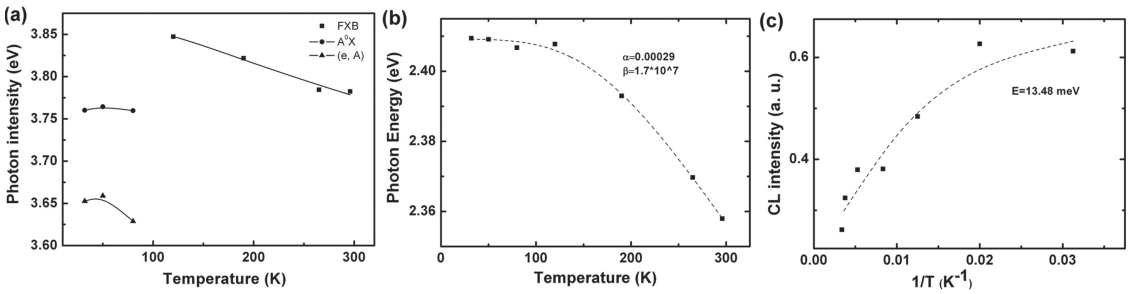

Figure 6. a) Temperature-dependent peak positions of FXB, A^0X and (e, A). b) Temperature-dependent peak positions around 514 nm and c) its corresponding integrated intensity as a function of reciprocal temperature.

$$E(T) = E(0) - \frac{\alpha T^4}{T^3 + \beta}$$

Good fitting results were obtained for 514 nm (2.412 eV) emission using the fitting parameters E_0 = 2.40915, α = 0.00029, and $\beta = 1.706 \times 10^7$.

Figure 6c shows the CL intensities of 514 nm band as a function of temperature, indicating that the CL intensities approximately follow an exponential decay with increasing temperature, as expected from the formula:[41]

$$I(T) = \frac{I_0}{1 + A\exp(-E_a/k_B T)}$$

Where I_0 is the intensity at zero absolute temperature, A a temperature independent constant, E_a the activation energy for thermal quenching processes, k_B the Boltzmann constant, and T the temperature in Kelvin. The activation energy E_a is 13.48 meV for this band, which may be related to the electrons escape from the isolated Zn vacancy to other energy levels and giving off its energy by nonradiative process.

CL is especially useful to characterize the optical properties of individual nanostructures due to its high spatial resolution. In order to study the morphology-dependent CL properties, the CL measurements were performed on different morphologies of individual 1D ZnS nanostructures, including regular and irregular shaped nanobelts and nanorods. Using the same characterization methods described in our previous work, the CL properties of individual ZnS nanobelts dispersed on standard C-coated TEM copper grids were studied using high-spatial-resolution SEM.[14] **Figure 7**a,b are the SEM and the corresponding CL images of a single nanobelt, showing its distinct shape which arises from the uniform luminescence. Figure 7c displays a pure ZnS nanobelt CL spectrum with a narrow and strong and sharp UV peak centered at 338 nm (3.669 eV) and a broad, low-density luminescence peak around 543 nm (2.284 eV). Figure 7d plots the CL spectra collected at different spots along the line as shown in the nanobelt. All peaks of different spots are located at the same wavelengths, while the intensities of the UV peak are slightly changed, also indicating that the luminescence is rather homogenous. This result is in good agreement with the good crystalline quality of the nanobelts.

It is well known that nanomaterials have large surface-to-volume ratios, and their physical properties are expected to be highly sensitive to surface quality and morphology. On the other hand, it is also important to investigate the properties of irregular shape if one wants to use them to construct nanodevices and utilize materials more efficiently. With the question of whether variations of morphology have direct effect on the CL properties, the CL spectra were collected on an individual ZnS nanobelt with irregular morphology, as shown in **Figure 8**. The CL image of Figure 8b suggests that the luminescence is also fairly uniform. Figure 8c are their corresponding CL spectra between 300 nm and 380 nm of different spots marked in Figure 8a. Compared with the CL spectra in Figure 3d, the peak positions changes from 332 nm (2.735 eV) to 337 nm (2.680 eV), while the intensities of UV emissions are very weak and vary from spot to spot, and similar phenomenon have also

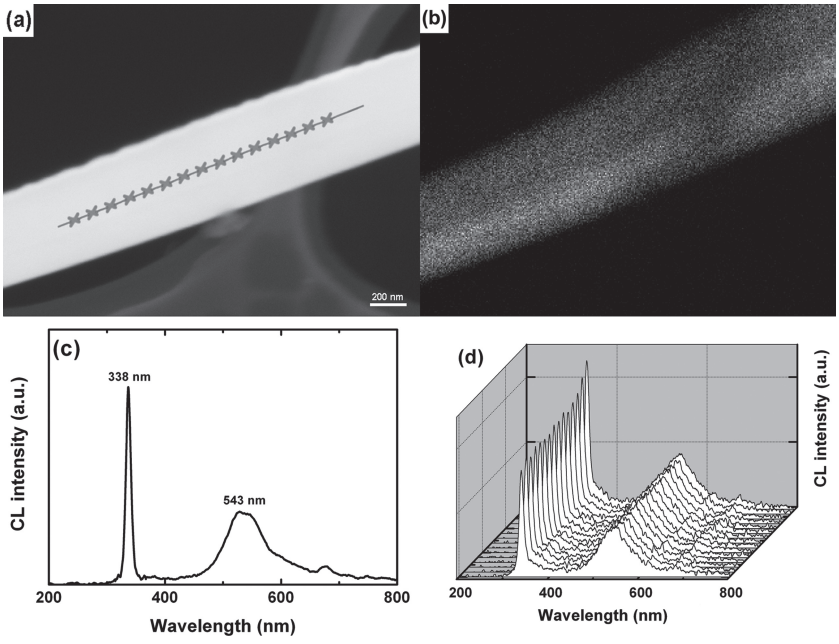

Figure 7. a) SEM image of a ZnS nanobelt. b) The corresponding CL image and c) CL spectrum. d) CL spectra collected at various spots on the nanobelt surface along the line marked in (a).

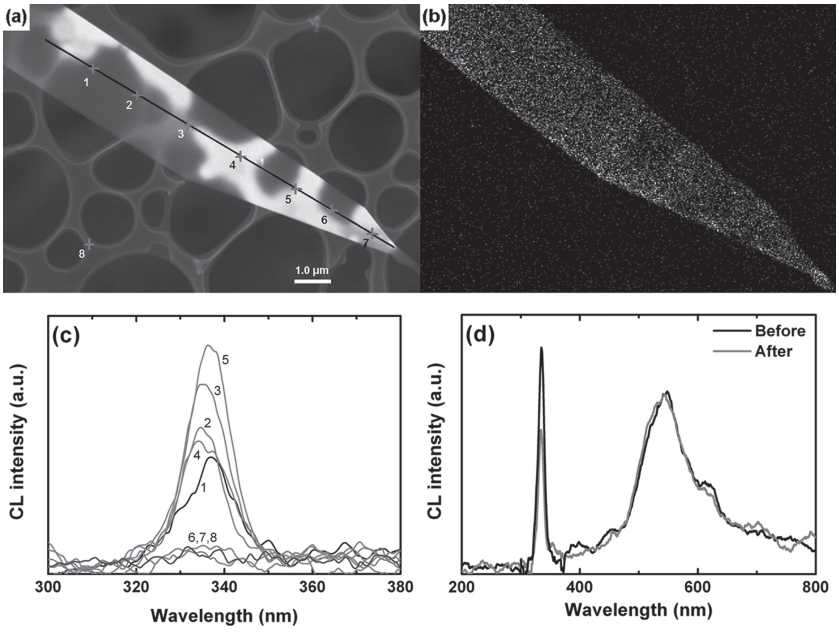

Figure 8. a) The recorded spots at an irregular shaped ZnS nanobelt and b) its corresponding CL image. c) CL spectra recorded from 300 nm to 380 nm at room temperature from spots marked in (a). d) The CL spectra of (a) before and after electron beam irradiation at 10 kV and 2000 pA.

been observed in previous work in ZnS nanowires.[24,26] The CL spectra of spot 6 and 7 are almost the same as the spot 8 which located the outside area of the nanobelt, the intensities decreasing to zero. This may be attributed to that the sample was shifted slightly during the measurement and the electron beam was focused on the outer space of the nanobelt after the CL observation. The spectra lines in Figure 8d were collected before and after the first CL spectrum collection of this nanobelt. It is easy to note that the emission of the visible band keeps unchanged, while the intensity of UV emission band slightly decreases. This kind of UV degradation was also observed in ZnO crystals under the electron beam irradiation, and may be due to some modifications near the surface introduced by the electron beam irradiation.[40] It seems that there is not so many difference of the CL properties at room temperature between the regular and irregular shaped nanobelts, indicating that these irregular shaped nanobelts may also show potential application on nanodevices.

For further confirming our assumption of this stable property, we do more measurements on some other different irregular shaped ZnS nanobelts, as shown in **Figure 9**. The CL image in Figure 9b exactly shows the shape of the nanobelt. Similar UV emissions are depicted in Figure 8c. The low intensity of spot 1 indicates that the electron beam on edge of the nanobelt may be shifted. **Figure 10** is the SEM image and CL spectra at different spots of a typical nanorod. It is also observed that the CL spectra show similar shapes but slightly difference of luminescent intensities compared to the nanobelts. This may be due to the different morphology that nanorods are much thicker than nanobelts, and also the surface states are different.

Doping is one of the common methods to endow compounds with other new properties. When semiconductors are doped with other elements, the band-gap can be altered. ZnS is a prime example because it is widely used in the lighting and display technique in order to obtain different color by doping with other elements and even fabricate composite with other compounds. The synthesis of Fe-doped and Fe/Mn-co-doped ZnS nanobelts and nanorods were the same as previous report,[28] and the structural and compositional characterizations can be referred therein. **Figure 11**a,b show the SEM image and their corresponding CL image recorded at 522 nm for Fe-doped nanobelts and nanorods, respectively. The SEM image and their corresponding CL image recorded at 580 nm for Fe/Mn-co-doped ZnS nanobelts and nanorods are shown in Figure 11d,e, respectively. Both of the CL spectra in Figure 10c,f show the UV band centered at 340 nm, and a broad visible band at 522 nm and 580 nm for Fe-doped and Fe/Mn-co-doped ZnS nanobelts and nanorods, respectively. The 522 nm emission is attributed to Fe doping, and 580 nm is associated with the $^4T_1 \rightarrow {}^6A_1$ transition in Mn^{2+}.[28] CL images in Figure 11b,e show almost uniform emissions at 522 nm for Fe-doped and at 580 nm for Fe/Mn-co-doped ZnS nanobelts and nanorods, which is in good aggrement with the EDS results that Fe/Mn doping is homogenous in the nanostructures. Compared with the former PL observations,[28] the shape and peak positions are almost the

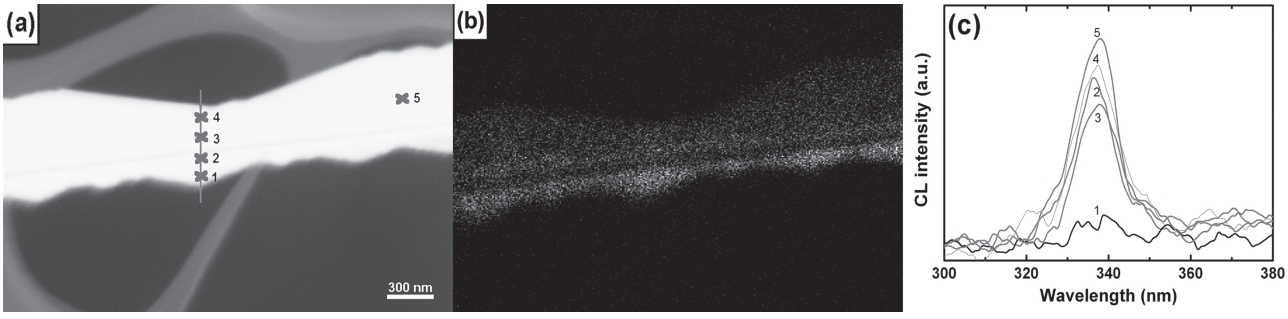

Figure 9. a) SEM image of another irregular shaped ZnS nanobelt and b) its corresponding CL image. c) CL spectra acquired at various spots marked in (a).

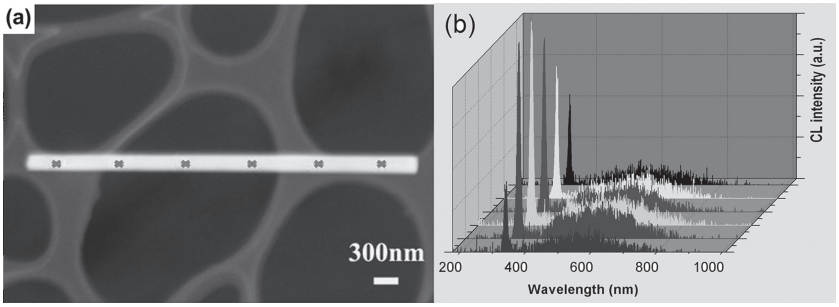

Figure 10. a) SEM image of an individual ZnS nanorod and b) the corresponding CL spectra acquired at various spots marked in (a).

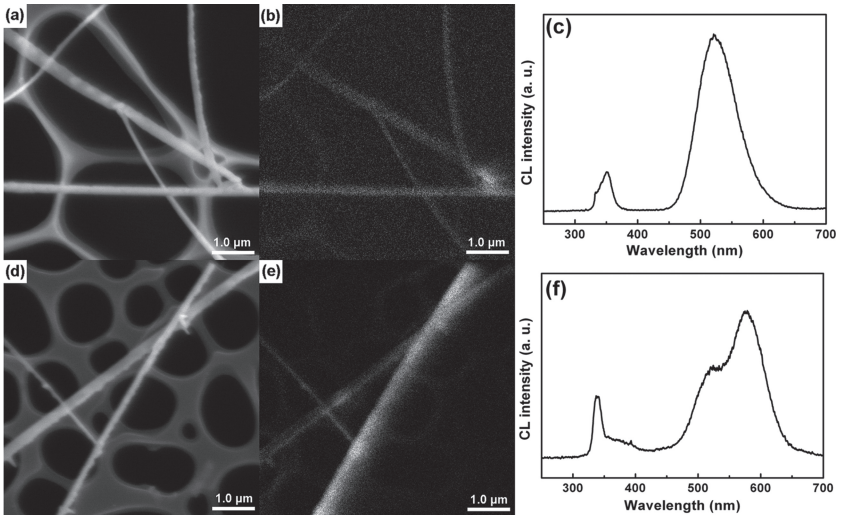

Figure 11. a,d) SEM images of Fe-doped and Fe/Mn-co-doped ZnS nanobelts. b,e) The corresponding CL images shown in (a) and (d). c,f) CL spectra.

same. However, the relative intensity ratio between UV and visible peak are lower, indicating that there is a difference in the defects (less shallow levels-related, deeper ones).[23]

3. Conclusion

Morphology, doping and temperature-dependent cathodoluminescence modulation of 1D ZnS nanostructures were performed in the present study. All 1D ZnS nanostructures exhibit sharp UV band-gap emission at room temperature. 32 K CL analysis of nanobelts was further performed, which consists of a narrow and strong UV peak and two broad, low-intensity emissions in the visible region. Temperature-dependent CL from such single-crystalline ZnS nanobelts in the temperature range of 32 to 296 K and Gaussian fitting show two UV peaks of 3.757 eV and 3.646 eV, which can be attributed to the recombination of exciton bond to a neutral acceptor (A^0X) and from free electrons in the conduction band to an acceptor level (e, A), respectively. No difference of the CL properties has been detected from both regular and irregular shaped nanobelts at room temperature. The effect of Fe doping and Fe/Mn co-doping on CL property of ZnS nanobelts and nanorods indicates that there is a difference between CL and PL in the defects emissions of 1D ZnS nanostructures. These ZnS nanostructures show potential applications in luminescent materials as well as short-wavelength nanolaser light sources.

4. Experimental Section

High quality ZnS nanobelts and nanorods were synthesized on an Au-coated Si substrate and an Au-coated GaAs substrate via a facile thermal evaporation route, respectively. The growth of ZnS nanobelts was prepared using a method similar with our previously reported one with minor modification on synthesis conditions: a precursor of high-purity commercial ZnS powder (≈10 mm, 99.99%) was loaded at the center of a horizontal tube furnace.[14] Silicon substrates regardless of the growth direction coated with a thin layer of Au catalyst (3 nm thickness) were placed at the downstream position of high-purity commercial ZnS powder. The furnace was heated to 1100 °C in 1 h and kept for 45 min with a constant high-purity argon (Ar) gas flow of 120 sccm (standard cubic centimeter per minute). The synthesis of ZnS nanorods was achieved by adopting GaAs (111) wafer coated with 3 nm thick Au catalyst layer as a growth substrate. The growth temperature was decreased to 850 °C while all the other conditions kept the same as in the growth of ZnS nanobelts. The thin layer of Au catalyst was prepared using an electric gun deposition system (ULVAC UEP-3000-2C) at an evaporation rate of 0.01 Å/s. The synthesis of Fe-doped and Fe/Mn-co-doped ZnS nanobelts were reported in ref. [28], in which ZnO powder (99.99%, Sigma-Aldrich) was used instead of ZnS powder and FeS powder (99.9%, Sigma-Aldrich) and $FeCl_2$ beads (99.998%, Sigma-Aldrich) were used for Fe-doping and FeS powder, and $MnCl_2$ (99.999%, Sigma-Aldrich) beads were used for Fe/Mn-co-doping, respectively.

The prepared ZnS nanostructures were characterized using a field-emission scanning electron microscope (SEM, JSM-6700F) and a transmission electron microscope (TEM, JEOL 2010) equipped with an X-ray energy dispersive spectrometer (EDS). After the structural and chemical examinations, spatially resolved CL spectra from individual ZnS nanostructures with diverse morphologies or their assemblies were collected with a high-resolution CL system at an accelerating voltage of 10 kV and at a constant current of 2,000 pA at room temperature using an Ultra-High Vacuum SEM and a Gemini electron gun (Omicron) equipped with a CL system. Temperature-dependent CL from single-crystalline ZnS nanobelts in the temperature range of 32 to 296 K was observed in a field emission (FE)-SEM (S6600, Hitachi) equipped with a CL system.

Acknowledgements

This work was supported by the National Natural Science Foundation of China (Grant Nos. 91123006, 21001028 and 51002032), the National Basic Research Program of China (Grant No. 2012CB932303), Shanghai Chenguang Foundation (11CG06), Shanghai Pujiang Program (11PJ1400300, 12PJ1400300), Shanghai Shu Guang Project, Science and Technology Commission of Shanghai Municipality (11520706200),

the Scientific Research Foundation for the Returned Overseas Chinese Scholars, State Education Ministry, and the Programs for Professor of Special Appointment (Eastern Scholar) at Shanghai Institutions of Higher Learning and for New Century Excellent Talents in University (NCET-11-0102).

Received: December 15, 2012
Published online: March 5, 2013

[1] a) T. Palacios, *Nature* **2012**, *481*, 152; b) R. S. Devan, R. A. Patil, J. H. Lin, Y. R. Ma, *Adv. Funct. Mater.* **2012**, *22*, 3326; c) L. F. Hu, J. Yan, M. Y. Liao, H. J. Xiang, X. G. Gong, L. D. Zhang, X. S. Fang, *Adv. Mater.* **2012**, *24*, 2305.

[2] a) Z. Y. Fan, J. C. Ho, T. Takahashi, R. Yerushalmi, K. Takei, A. C. Ford, Y. L. Chueh, A. Javey, *Adv. Mater.* **2009**, *21*, 3730; b) Z. Y. Wang, X. W. Lou, *Adv. Mater.* **2012**, *24*, 4124.

[3] a) L. Li, Y. W. Yang, G. H. Li, L.D. Zhang, *Small* **2006**, *2*, 548; b) S. L. Ji, C. H. Ye, *J. Mater. Sci. Technol.* **2008**, *24*, 457; c) X. S. Fang, J. Yan, L. F. Hu, H. Liu, P. S. Lee, *Adv. Funct. Mater.* **2012**, *22*, 1613.

[4] a) L. Li, H. Lu, Z. Y. Yang, L. M. Tong, Y. Bando, D. Golberg, *Adv. Mater.* **2012**, DOI: 10.1002/adma.201204434; b) H. C. Wu, Y. C. Huang, I. K. Ding, C. C. Chen, Y. H. Yang, C. C. Tsai, C. D. Chen, Y. T. Chen, *Adv. Funct. Mater.* **2011**, *21*, 474; c) X. S. Fang, L. M. Wu, L. F. Hu, *Adv. Mater.* **2011**, *23*, 585.

[5] a) X. S. Fang, L. F. Hu, K. F. Huo, B. Gao, L. J. Zhao, M. Y. Liao, P. K. Chu, Y. Bando, D. Golberg, *Adv. Funct. Mater.* **2011**, *21*, 3907; b) Y. Liang, H. Liang, X. D. Xiao, S. K. Hark, *J. Mater. Chem.* **2012**, *22*, 1199.

[6] a) J. Tang, Z. Huo, S. Brittman, H. Gao, P. Yang, *Nat. Nanotechnol.* **2011**, *6*, 568; b) S. K. Kim, R. W. Day, J. F. Cahoon, T. J. Kempa, K. D. Song, H. G. Park, C. M. Lieber, *Nano Lett.* **2012**, *12*, 4971.

[7] a) A. Menzel, K. Subannajui, F. Güder, D. Moser, O. Paul, M. Zacharias, *Adv. Funct. Mater.* **2011**, *21*, 4342; b) L. D. Zhang, M. Fang, *Nano Today* **2010**, *5*, 128.

[8] a) W. L. Davidson, *Phys. Rev.* **1948**, *74*, 116; b) L. D. DeLoach, R. H. Page, G. D. Wilke, S. A. Payne, W. F. Krupke, *IEEE J. Quantum Electron.* **1996**, *32*, 885; c) R. H. Page, K. I. Schaffers, L. D. DeLoach, G. D. Wilke, F. D. Patel, J. B. Tassano Jr., S. A. Payne, W. F. Krupke, K. T. Chen, A. Burger, *IEEE J. Quantum Electron.* **1997**, *33*, 609; d) S. Peralta, H. Tuda, *IEEE Ind. Appl. Mag.* **1998**, *4*, 31.

[9] a) U. K. Gautam, X. S. Fang, Y. Bando, J. H. Zhan, D. Golberg, *ACS Nano* **2008**, *2*, 1015; b) X. S. Fang, U. K. Gautam, Y. Bando, D. Golberg, *J. Mater. Sci. Technol.* **2008**, *24*, 520; c) X. S. Fang, C. H. Ye, L. D. Zhang, Y. H. Wang, Y. C. Wu, *Adv. Funct. Mater.* **2005**, *15*, 63.

[10] Y. Ding, X. D. Wang, Z. L. Wang, *Chem. Phys. Lett.* **2004**, *398*, 32.

[11] D. Moore, Z. L. Wang, *J. Mater. Chem.* **2006**, *16*, 3898.

[12] D. Moore, Y. Ding, Z. L. Wang, *J. Am. Chem. Soc.* **2004**, *126*, 14372.

[13] Z. W. Wang, L. L. Daemen, Y. S. Zhao, C. S. Zha, R. T. Downs, X. D. Wang, Z. L. Wang, R. J. Hemley, *Nat. Mater.* **2005**, *4*, 922.

[14] X. S. Fang, Y. Bando, M. Y. Liao, U. K. Gautam, C. Y. Zhi, B. Dierre, B. D. Liu, T. Y. Zhai, T. Sekiguchi, Y. Koide, D. Golberg, *Adv. Mater.* **2009**, *21*, 2034.

[15] X. S. Fang, Y. Bando, M. Y. Liao, T. Y. Zhai, U. K. Gautam, L. Li, Y. Koide, D. Golberg, *Adv. Funct. Mater.* **2010**, *20*, 500.

[16] a) Z. G. Chen, L. N. Cheng, H. Y. Xu, J. Z. Liu, J. Zou, T. Sekiguchi, G. Q. Lu, H. M. Cheng, *Adv. Mater.* **2010**, *22*, 2376; b) X. S. Fang, Y. Bando, G. Z. Shen, C. H. Ye, U. K. Gautam, P. M. F. J. Costa, C. Y. Zhi, C. C. Tang, D. Golberg, *Adv. Mater.* **2007**, *19*, 2593.

[17] a) L. Sorensen, G. F. Strouse, A. E. Stiegman, *Adv. Mater.* **2006**, *18*, 1965; b) L. F. Lu, F. J. Zhang, Z. Xu, S. L. Zhao, Z. L. Zhuo, D. D. Song, J. M. Li, Y. S. Wang, *Physica B* **2010**, *405*, 3728.

[18] a) J. W. Moreau, P. K. Weber, M. C. Martin, B. Gilbert, I. D. Hutcheon, J. F. Banfield, *Science* **2007**, *316*, 1600; b) X. S. Fang, T. Y. Zhai, U. K. Gautam, L. Li, L. M. Wu, Y. Bando, D. Golberg, *Prog. Mater. Sci.* **2011**, *56*, 175.

[19] a) H. Yang, P. H. Holloway, *Adv. Funct. Mater.* **2004**, *14*, 152; b) H. Z. Wang, H. Nakamura, M. Uehara, Y. Yamaguchi, M. Miyazaki, H. Maeda, *Adv. Funct. Mater.* **2005**, *15*, 603.

[20] T. Mitsui, N. Yamamoto, T. Tadokoro, S. Ohta, *J. Appl. Phys.* **1996**, *80*, 6972.

[21] B. G. Yacobi, D. B. Holt, *J. Appl. Phys.* **1986**, *59*, R1.

[22] P. R. Edwards, R. W. Martin, *Semicond. Sci. Technol.* **2011**, *26*, 064005.

[23] B. Dierre, X. L. Yuan, T. Sekiguchi, *Sci. Technol. Adv. Mater.* **2010**, *11*, 043001.

[24] D. D. D. Ma, S. T. Lee, P. Mueller, S. F. Alvarado, *Nano Lett.* **2006**, *6*, 926.

[25] a) R. Chen, D. H. Li, B. Liu, Z. P. Peng, G. G. Gurzadyan, Q. H. Xiong, H. D. Sun, *Nano Lett.* **2010**, *10*, 4956; b) Q. H. Xiong, G. Chen, J. D. Acord, X. Liu, J. J. Zengel, H. R. Gutierrez, J. M. Redwing, L. C. L. Y. Voon, B. Lassen, P. C. Eklund, *Nano Lett.* **2004**, *4*, 1663.

[26] X. S. Fang, U. K. Gautam, Y. Bando, B. Dierre, T. Sekiguchi, D. Golberg, *J. Phys Chem C* **2008**, *112*, 4735.

[27] Y. Jiang, W. J. Zhang, J. S. Jie, X. M. Meng, J. A. Zapien, S. T. Lee, *Adv. Mater.* **2006**, *18*, 1527.

[28] T. Kang, J. Sung, W. Shim, H. Moon, J. Cho, Y. Jo, W. Lee, B. Kim, *J. Phys. Chem. C* **2009**, *113*, 5352.

[29] H. Y. Wang, C. R. Wang, J. Xu, X. Liu, X. F. Xu, H. Z. Xing, L. J. Zhao, X. S. Chen, *J. Phys. D Appl. Phys.* **2012**, *45*, 095301.

[30] C. H. Ye, X. S. Fang, M. Wang, L. D. Zhang, *J. Appl. Phys.* **2006**, *99*, 063504.

[31] Y. Wang, L. D. Zhang, C. H. Liang, G. Z. Wang, X. S. Peng, *Chem. Phys. Lett.* **2002**, *357*, 314.

[32] a) M. Hafeez, T. Y. Zhai, A. S. Bhatti, Y. Bando, D. Golberg, *J. Phys. Chem. C* **2012**, *116*, 8297; b) L. W. Yin, Y. Bando, J. H. Zhan, M. S. Li, D. Golberg, *Adv. Mater.* **2005**, *17*, 1972; c) Y. C. Zhu, Y. Bando, D. F. Xue, *Appl. Phys. Lett.* **2003**, *82*, 1769.

[33] Q. Li, C. R. Wang, *Appl. Phys. Lett.* **2003**, *83*, 359.

[34] T. K. Tran, W. Park, W. Tong, M. M. Kyi, B. K. Wagner, C. J. Summers, *J. Appl. Phys.* **1997**, *81*, 2803.

[35] S. Nam, B. Oyungsung, K. S. Lee, Y. D. Choi, C. S. Kim, *J. Appl. Phys.* **1998**, *84*, 1047.

[36] S. Nam, J. Rhee, Y. M. Yu, B. Oyungsung, K. S. Lee, Y. D. Choi, *Mater. Chem. Phys.* **1998**, *55*, 229.

[37] J. H. Zhan, Y. Bando, J. Q. Hu, D. Golberg, *Appl. Phys. Lett.* **2006**, *89*, 243111.

[38] F. Banhart, *Rep. Prog. Phys.* **1999**, *62*, 1181.

[39] B. D. Liu, Y. Bando, M. S. Wang, C. Y. Zhi, X. S. Fang, *J. Appl. Phys.* **2009**, *106*, 034302.

[40] B. Dierre, X. L. Yuan, Y. Z. Yao, M. Yokoyama, T. Sekiguchi, *J Mater Sci: Mater Electron* **2008**, *19*, S307.

[41] H. Lei, H. S. Leipner, V. Bondarenko, J. Schreiber, *J. Phys.: Condens. Matter* **2004**, *16*, S279.